

AI-Based Detection of In-Treatment Changes from Prostate MR-Linac Images

Seungbin Park¹, Peilin Wang¹, Ryan Pennell², Emily S. Weg²,
 Himanshu Nagar³, Timothy McClure¹, Mert R. Sabuncu^{1,4}, Daniel Margolis¹, Heejong Kim^{1*}

hkim@med.cornell.edu

¹Radiology, Weill Cornell Medicine, New York, NY 10065

²Radiation Oncology, Weill Cornell Medicine, New York, NY 10065

³Department of Radiation Oncology, Memorial Sloan Kettering Cancer Center, New York, NY 10065

⁴School of Electrical and Computer Engineering, Cornell University and Cornell Tech, New York, NY 10044

Abstract

Purpose: To investigate whether routinely acquired longitudinal MR-Linac images can be leveraged to characterize treatment-induced changes during radiotherapy, particularly subtle inter-fraction changes over short intervals (average of 2 days).

Materials and Methods: This retrospective study included a series of 0.35T MR-Linac images from 761 patients. An artificial intelligence (deep learning) model was used to characterize treatment-induced changes by predicting the temporal order of paired images. The model was first trained with the images from the first and the last fractions (F_1 - F_L), then with all pairs (All-pairs). Model performance was assessed using quantitative metrics (accuracy and AUC), compared to a radiologist's performance, and qualitative analyses—the saliency map evaluation to investigate affected anatomical regions. Input ablation experiments were performed to identify the anatomical regions altered by radiotherapy. The radiologist conducted an additional task on partial images reconstructed by saliency map regions, reporting observations as well. Quantitative image analysis was conducted to investigate the results from the model and the radiologist.

Results: The F_1 - F_L model yielded near-perfect performance (AUC of 0.99), significantly outperforming the radiologist. The All-pairs model yielded an AUC of 0.97. This performance reflects therapy-induced changes, supported by the performance correlation to fraction intervals, ablation tests and expert's interpretation. Primary regions driving the predictions were prostate, bladder, and pubic symphysis.

Conclusion: The model accurately predicts temporal order of MR-Linac fractions and detects radiation-induced

changes over one or a few days, including prostate and adjacent organ alterations confirmed by experts. This underscores MR-Linac's potential for advanced image analysis beyond image guidance.

Abbreviations

EBRT = external beam radiotherapy, RT = radiation therapy, MRI = magnetic resonance imaging, MR-Linac = Magnetic Resonance-Linear Accelerator, ADC = apparent diffusion coefficient, AI = artificial intelligence, AUC = area under the receiver operation characteristic curve, CI = confidence interval, PSA = prostate-specific antigen, ADT = androgen deprivation therapy

Summary

MR images from MR-Linac fractions contain therapy-induced changes that can be systematically detected using artificial intelligence.

Key Points

1. An artificial intelligence model accurately determined the temporal order of images from MR-Linac fractions, exceeding human expert performance and demonstrating the presence of radiation therapy-related changes.
2. Radiation therapy-induced changes were most pronounced in the prostate, with additional contributions from the bladder and surrounding pelvic tissues, supporting the clinical value of MR-Linac imaging for treatment monitoring.

Keywords

Prostate Cancer, MR-Linac, Radiation Therapy, Longitudinal Image Analysis, Adaptive Radiotherapy, Deep Learning, Artificial Intelligence

*Corresponding author.

1. Introduction

A common therapeutic strategy for prostate cancer patients is external beam radiotherapy (EBRT), delivered either independently or in combination with surgery or hormone therapy [17, 18]. Image-guided radiation therapy (RT) has become standard practice for ensuring precise localization of the target and safe treatment delivery. Magnetic Resonance-Linear Accelerator (MR-Linac) systems combine MRI with a linear accelerator, enabling the acquisition of high-soft-tissue-contrast MR images at every treatment fraction [20, 22]. This integration allows visualization of the prostate, bladder, rectum, and adjacent tissues before radiation delivery and day-to-day anatomical changes throughout the treatment course [19, 20, 22]. Moreover, the MR images allow for adaptive therapy taking inter- and intra-fraction motion management into account, modifying each treatment fraction as needed based on spatiotemporal variations to ensure maximal target dose delivery with minimal dose to adjacent organs [7, 15, 22, 25].

While MR-Linac provides unprecedented access to longitudinal MR imaging throughout the treatment course, potential treatment-induced changes in the images have been unexplored. This is due to the relatively poor image quality and the subtle changes that are challenging for human observers to detect, combined with the fact that these images are primarily used for guiding RT and rarely reviewed beyond gross anatomical assessment. As a result, despite their potential clinical relevance for adaptive planning, treatment personalization, and toxicity prediction, systematic characterization of fraction-to-fraction changes remains limited [7].

Several studies have reported significant prostate volume changes in diagnostic-quality MR images during a course of RT [1, 17]. Longitudinal studies using multiparametric MRI [2, 9] and quantitative MRI [27] have demonstrated changes in prostate tumors and/or surrounding tissues before and after treatment delivery. From MR-Linac images, prior works have shown changes in apparent diffusion coefficient (ADC) [3, 8]. These prior studies suggest that MR imaging during RT can capture dynamic, patient-specific morphological and tissue changes. However, to the best of our knowledge, inter-fraction changes in routinely acquired MR-Linac RT imaging have not been previously studied.

In this study, we developed an AI (artificial intelligence) model designed to detect subtle changes in MR images from MR-Linac fractions in one or a few days, adapting a longitudinal image comparison framework [13]. We hypothesized that a model capable of accurately ordering images chronologically would rely on features that evolve consistently with cumulative radiation exposure. The model achieved over 95% accuracy, substantially outperforming an expert, and identified prostate and surrounding anatomical structures, such as bladder and pubic symphysis, as key regions

driving radiation-induced changes. These findings are supported by input ablation experiments and quantitative image analysis. Overall, our study suggests that beyond its established role in patient alignment and dose planning, MR-Linac imaging can be leveraged to study longitudinal, treatment-induced changes during RT, providing AI-derived imaging features that may support treatment monitoring and adaptation.

2. Materials and Methods

2.1. Data

The study is HIPAA-compliant and IRB-approved with a waiver of informed consent for retrospective studies. All data were de-identified prior to analysis.

We retrospectively collected 1,071 patients who underwent MR-guided RT from 2018 to 2025, screened to 761 patients for the study (Details of selection are in the Supplementary Section A1 and flow diagram is in Supplementary Figure A1). The images include simulation scans (*Sim* in Figure 1A) and corresponding treatment fractions (F_1 to F_n in Figure 1A)), with inter-fraction intervals of one day or more (Supplementary Figure A2). All images were acquired using a ViewRay MRIdian MR-Linac system (ViewRay Inc., USA) equipped with a 0.35-T MRI, using True Fast Imaging with Steady-State Free Precession (TRUFPI) sequence. The in-plane pixel spacing was $1.5 \times 1.5 \text{ mm}^2$, with a slice thickness of 1.5 or 3 mm. Apart from cropping centered on prostate masks (see Supplementary Section A2 for segmentation method) to (80, 80, 80) sized volumes, no further pre-processing was performed.

Data were randomly split on a patient-wise basis into training (60%, $n = 457$), validation (20%, $n = 152$), and test data (20%, $n = 152$). All MR images were cropped to dimensions of (80, 80, 80), centered at the centroid of the prostate mask (see Supplementary Section A2 for segmentation method).

2.2. Model

The overall framework (Figure 1B) is based on learning-based Inference of Longitudinal imAge Changes (LILAC) [13], which learns meaningful changes from paired longitudinal images via predicting temporal order. As temporal ordering has demonstrated effectiveness in capturing monotonic changes, we adopted it to identify features consistently changing over the course of treatment. We employed a Siamese 3D convolutional neural network [5, 6, 12] with ResNet-18 [10] architecture. The model outputs logits for binary classification, predicting whether the input pair is in the correct or reversed temporal order. These logits reflect the model's confidence, informed by learned differences between paired longitudinal images. Code is provided in <https://github.com/anonymized/mr-linac>

[ai/will_be_added](#). Further details are available in Supplementary Section A3.

For training, MR images from multiple fractions were paired in all possible ordered permutations. A curriculum learning was adopted, where initial training used only first-last fraction image pairs (F_1 – F_L pairs), which exhibit the largest radiation-induced differences and are therefore easier to learn [4]. The model was further trained using all combinations of image pairs (All pairs; All-pairs model), with parameters initialized from those of the best F_1 – F_L model. More details are in Supplementary Section A4.

2.3. Assessment of Changes Across Fractions via Model Performance

The held-out test data (152 patients, 732 image pairs) were used to evaluate the performance across all experiments.

Temporal ordering performance evaluation.— Model performance was assessed using accuracy and the area under the receiver operating characteristic curve (AUC), with confidence intervals (CI) obtained from 1,000 bootstrap resamples of the test data.

Comparison to expert: A radiologist with over 15 years of experience performed pairwise image comparison task to identify the correct order for the same F_1 – F_L pairs.

Sim-F1 test: As Sim and F_1 images are acquired before treatment, these pairs (Sim - F_1) were used to evaluate the model’s sensitivity to radiation-induced changes rather than temporal changes alone.

Fraction-pairwise performance evaluation.— As shown in Kim et al. [12], the model output reflects the magnitude of changes between image pairs. Based on this observation, we examined logits of the All-pairs model across fraction levels. To further quantify the relationship between fraction intervals and logits, we computed the Pearson correlation coefficient and fit a linear mixed-effects model with patient as a random effect (See Supplementary Section A5 for more details).

2.4. Identification of Anatomical Regions with Changes Across Fractions Using Model

Saliency map.— Saliency maps highlight regions that the model identifies as contributing most strongly to the differences between a given image pair, which are likely to reflect RT-induced effects. We used a modified Gradient-weighted Class Activation Mapping (Grad-CAM) [13, 23] to calculate the saliency maps. Implementation details and population-level visualization on an atlas are available in Supplementary Section A6.

Input ablation.— Input ablation experiments were conducted to identify regions critical for the model’s prediction

by examining model performance changes depending on input changes (Figure 1). Occlusion was performed using either the segmented regions (see Supplementary Section A2 for segmentation method) themselves (*organ-masked-MR* input) or bounding boxes surrounding the segmented areas (*box-masked-MR* input), where lower performance indicates stronger model reliance on the occluded organ regions. Preservation was performed by retaining only the prostate, bladder, or both segmented regions in the MR images (*only-organ-MR* input), where higher performance indicates stronger model reliance on the preserved organ regions. These ablated inputs retain both organ size and intensity. To further assess the decoupled effect of organ size from intensity, segmented organ masks (prostate, bladder, or both) were used (*mask* input).

Expert Saliency-Restricted MR Evaluation The radiologist performed the same temporal-order identification task using images restricted to the regions highlighted by the saliency maps, with the saliency maps themselves not shown (*saliency-restricted-MR*; implementation details in Supplementary Section A7). The radiologist also documented the rationale for each decision. The overlaid saliency maps were later provided for expert’s evaluation in order to interpret the model’s decision-making process and explain regions affected by RT.

2.5. Image Analysis

Quantitative image analysis was performed to further investigate RT-induced changes and to compare them with the model and expert evaluations. Changes in organ volume, and in the mean and standard deviation of image intensity for the prostate and bladder were assessed for all patients between F_1 and F_L . Prostate and bladder were defined using inferred masks generated by the nnU-Net model (Supplementary Section A2).

2.6. Statistical Analysis

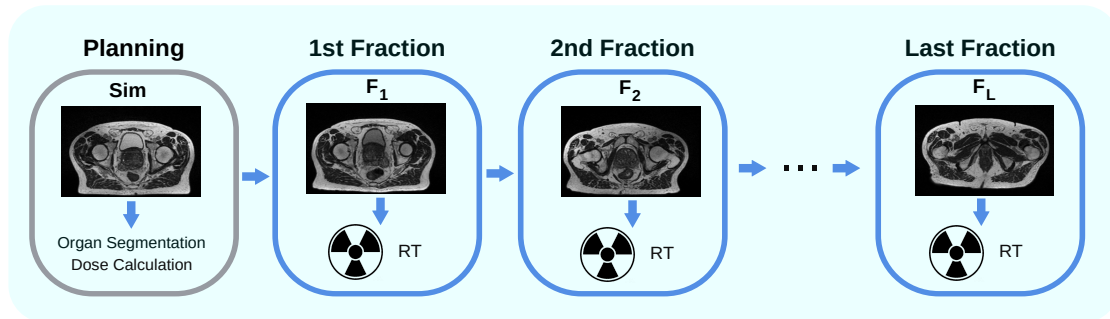
An independent two-sided t-test was conducted for comparisons of scores (accuracy and AUC) and patient characteristics. The Wilcoxon signed-rank test was used to compare organ volume and intensity from F_1 to F_L . For all statistical tests, p-value of 0.05 was used as the threshold for statistical significance. See Supplementary Section A8 for details on the tools used.

3. Results

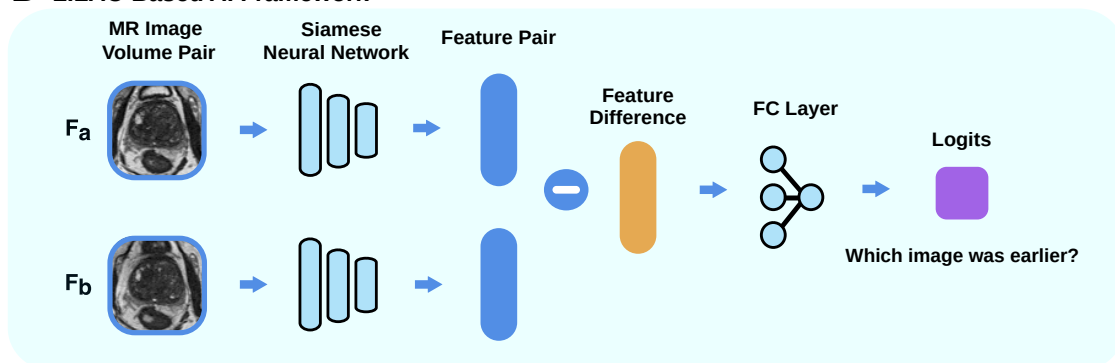
3.1. Patient Characteristics

All patients in the cohort (Table 1) were diagnosed with elevated prostate-specific antigen (PSA) levels and prostate cancer. All patients except 43 patients received five fractions of MR-Linac treatment, mostly administered every

A MR-LINAC Sessions



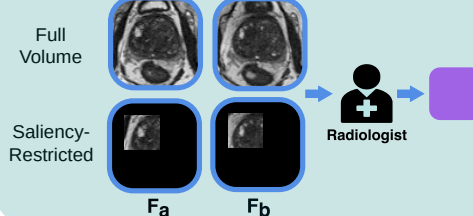
B LILAC-Based AI Framework



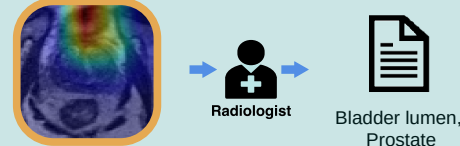
C Evaluation

Expert Evaluation

Prediction Test: Is the order correct?



Saliency map interpretation



Model Input Ablation

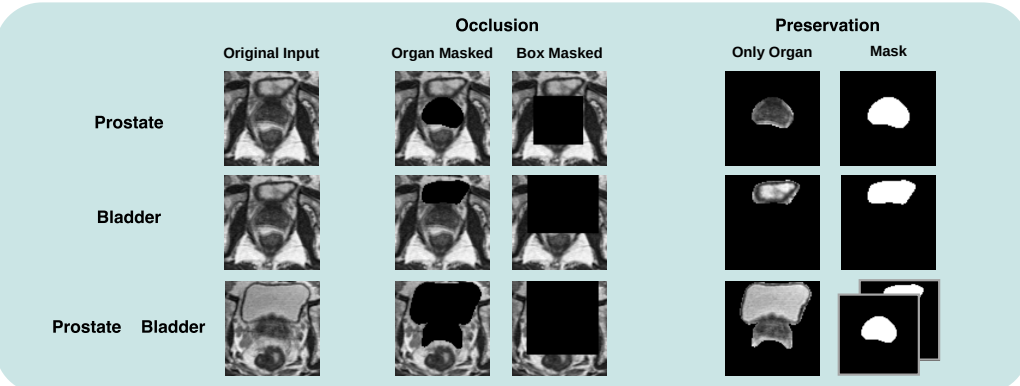


Figure 1. Overview of the MR-Linac workflow and AI framework.

Figure 1. (Continued) (A) Process of MR-Linac sessions across multiple fractions. *Sim* refers to the simulation scans obtained prior to MR-Linac treatment sessions. F_1, F_2, \dots, F_L represent MR images acquired at the first, second, ..., and last fractions, respectively, prior to image-guided radiation therapy (RT). (B) Schematic diagram of the LILAC-based AI model. Paired 3D MR image volumes from fractions are input to a Siamese 3D convolutional neural network with ResNet-18 [10] architecture, in which features of each image are obtained. The differences between these two features are fed into a fully connected layer. The logits are used for binary classification to predict if the image pairs are in the correct temporal order or not. (C) Experimental design for evaluation. A radiologist performed the same temporal-ordering task first with full volumes and next with saliency-restricted images. The radiologist also evaluated anatomical regions highlighted by the saliency maps. Model input ablation experiments were designed to evaluate altered anatomical regions. Performance changes when the prostate, bladder, or both regions or the surrounding box regions were masked in MR images (Organ Masked, Box Masked) were evaluated, as well as performance for partial MR images encompassing the organ regions (Only Organ). Performance for using only masks (Mask) was evaluated to investigate the effects of the organ shapes, compared to MR intensities.

| Characteristic | Training Data | Validation Data | Test Data |
|------------------------------|---------------|-----------------|--------------|
| No. of patients | 457 | 152 | 152 |
| Age (y) | 73 (10) | 73 (11) | 72.5 (10.25) |
| No. of fractions per patient | 5 (0) | 5 (0) | 5 (0) |
| Days between fractions | 2 (1) | 2 (1) | 2 (1) |
| PSA level (ng/mL) | 2.36 (4.38) | 2.13 (4.02) | 2.21 (2.59) |
| No. of patients with ADT | 180 (39) | 66 (43) | 55 (36) |

Note.—Age, the number of fractions per patient, days between fractions, and PSA level are reported as medians with interquartile ranges in parentheses. The number of patients with ADT is reported as medians with percentages in parentheses. No significant differences were found among values from the training, validation, and test data, except for the number of patients (independent two-sided t-test).

Table 1. Patient Characteristics.

| Pair | Performer | ACC | AUC |
|------------------|---|--------------------------|--------------------------|
| F_1-F_L | AI | 0.95 (0.93, 0.98) | 0.99 (0.99, 1.00) |
| | Expert | 0.82 (0.75, 0.87)* | - |
| <i>All-pairs</i> | AI | 0.91 (0.90, 0.92) | 0.97 (0.96, 0.97) |
| | AI, inference for <i>Sim-F</i> ₁ pairs | 0.39 (0.34, 0.45)* | 0.34 (0.28, 0.40)* |

Note.—* Significantly different from the bolded results (independent two-sided t-test, $p < .0001$)

Table 2. Performance of the model and the expert.

two days (Supplementary Figure A2). Approximately 40% of patients in the cohort underwent androgen deprivation therapy (ADT). There were no statistically significant differences between the train, validation, and test splits.

3.2. Evaluation of Changes in Images across Fractions via Model Performance

Because temporal order is inferred from image differences, output logits were used as a surrogate measure of change across RT fractions.

Model performance and comparative analysis.— The model performance on the test set was quantitatively evaluated (Table 2). The F_1-F_L model yielded the accuracy of 0.95 (95% CI: 0.93, 0.98), and the AUC of 0.99 (95% CI: 0.99, 1.00). The model outperformed the expert achieving

an accuracy of 0.82 (95% CI: 0.76, 0.88), of which the difference was statistically significant (independent two-sided t-test, $p < .0001$).

The *All-pairs* model achieved an accuracy of 0.95 (95% CI: 0.93, 0.97) and an AUC of 0.99 (95% CI: 0.99, 1.00). In contrast, inference on *Sim-F*₁ pairs yielded a significantly lower accuracy of 0.40 (95% CI: 0.34, 0.45) and AUC of 0.34 (95% CI: 0.28, 0.40) (independent two-sided t-test, $p < .0001$). The model achieved high accuracy on images acquired during RT but performed poorly on pre-RT images (*Sim-F*₁), indicating that RT-driven changes underlie the model's decisions. Patients who underwent ADT showed no statistically significant differences in model logits (independent two-sided t-test), further supporting that predictions are driven by RT-induced changes.

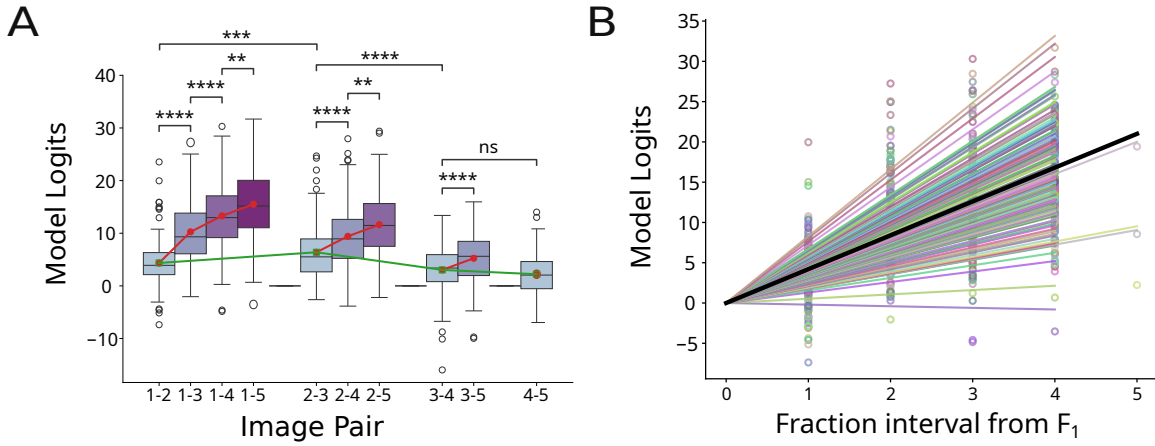


Figure 2. **Pairwise performance** (A) Model logits of the *All-pairs* model for different image pairs. Model logits reflect the model's confidence in its predictions, which can be interpreted as the magnitude of changes detected between paired images. Pairs of numbers on the x-axis indicate the fractions at which the paired images were acquired. Cases were grouped by the first fraction and ordered and color-coded by the interval between the paired fractions. Stars indicate statistical significance between compared cases (independent two-sided t-test; ns: $.05 < p < .05$, **: $.001 < p \leq .01$, ***: $.0001 < p \leq .001$, ****: $p \leq .0001$). Means within the same first fraction group are shown in red, whereas means with the same fraction interval but different first fraction groups are shown in green. (B) Linear mixed-effects model showing the relationship between fraction intervals from the first fraction and model logits (black), with patient-wise gradients shown in multicolor.

| Index | Expert Evaluation of Grad-CAM Peak | # of Cases |
|-------|---|-------------|
| 1 | Bladder lumen | 31 (20.53%) |
| 2 | Pubic symphysis | 29 (19.21%) |
| 3 | Bladder lumen, public symphysis, and periprostatic fascia (1 + 2 + 8) | 18 (11.92%) |
| 4 | Pubic symphysis and bladder lumen (1 + 2) | 17 (11.26%) |
| 5 | Base of prostate at urethral inlet | 8 (5.30%) |
| 6 | Public symphysis and base of prostate at urethral inlet (2 + 5) | 8 (5.30%) |
| 7 | Pubic symphysis and periprostatic fascia (2 + 8) | 7 (4.64%) |
| 8 | Periprostatic fascia | 6 (3.97%) |
| 9 | Bladder wall | 5 (3.31%) |
| 10 | Bladder lumen and lateral prostate (1 + 14) | 4 (2.65%) |
| 11 | Random fascia above the bladder | 4 (2.65%) |
| 12 | Urethral inlet and periprostatic fascia (5 + 8) | 3 (1.99%) |
| 13 | Bladder apex | 2 (1.32%) |

Note.—Regions with only one case are omitted from the table: prostate peripheral zone, pubic symphysis and lateral prostate possibly peripheral zone (2 + 14), anterior prostate and possibly artifact, pubic symphysis and tissue above bladder (2 + other), urethral inlet and bladder lumen (1 + 5), like 3 but ill-defined, ill-defined areas spanning the pubic symphysis and prostate base with additional bilateral areas in fascia above the bladder, periprostatic fascia and fascia above the bladder (8 + 11), and bladder lumen and periprostatic fascia (1 + 8).

Table 3. **Expert evaluation of peak regions of saliency maps from the *All-pairs* model on F_1-F_L pairs.**

Model performance on detecting RT-induced changes.—

Image differences between RT fractions are expected to increase with longer fraction intervals due to potential cumulative radiation exposure. To examine this, the performance of the *All-pairs* model for each fraction pair was evaluated (Figure 2 and Supplementary Figure A3). Model

logits were positively correlated with the inter-fraction interval (Pearson $r = 0.59, p < .0001$), as well as accuracy and AUC all increased proportionally with the fraction intervals (Supplementary Figure A3). Within groups of image pairs sharing the same first image (e.g. 1-2, 1-3, 1-4, and 1-5), the mean model logits increased with the fraction in-

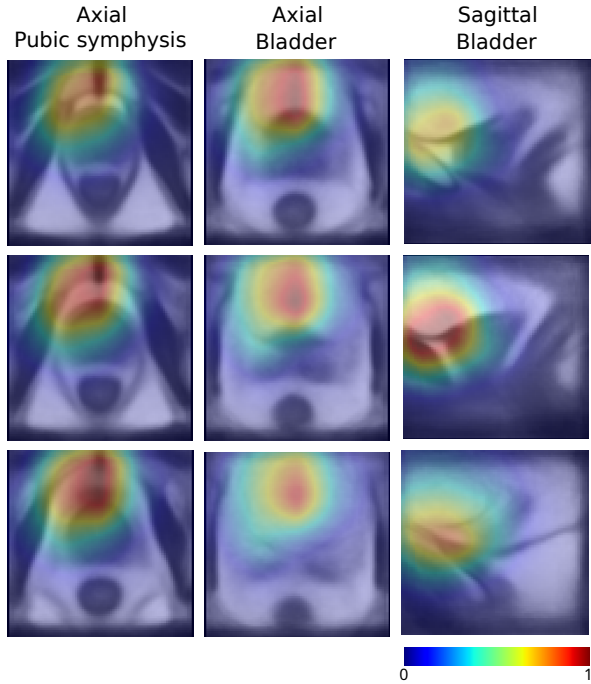


Figure 3. Saliency map on an atlas. The atlas was built from F_1 of all patients in the test data. The visualized heatmap is the mean of saliency maps for all patients in the test data, obtained from *All-pairs* model inference on F_1-F_L pairs and transformed into the atlas space. Column titles indicate the slice orientations (axial, sagittal) and the primary regions of interest highlighted by the saliency maps, although these regions span multiple organs.

terval (red lines in Figure 2A). Among adjacent image pairs (1-2, 2-3, 3-4, and 4-5), the F_2-F_3 pairs exhibited significantly higher than other one-interval pairs (green lines in Figure 2C), suggesting that RT-induced changes are most pronounced between the second and third fractions. These results demonstrate that the model predictions can quantify RT-induced changes between fractions.

Incorporating individual variability in the linear mixed-effects model resulted in a significant difference from the reduced model without random effects, according to the likelihood ratio test ($p < .0001$) (Figure 2). This indicates that the changes vary across patients, suggesting heterogeneous treatment effects.

3.3. Localization of RT-induced changes driving model predictions

Saliency Map.— Modified Grad-CAM[12, 23] based saliency maps were used to interpret which regions contribute to the model’s predictions. According to the radiologist’s evaluation, the saliency peaks most frequently occurred in the bladder lumen (20.53%) and pubic symphysis (19.21%), with the prostate commonly involved (Table 3). Group-level visualization of the heatmaps on the atlas of

all patients is shown in Figure 3 (Peak distribution of the heatmaps in Supplementary Figure A4), of which the primary peak regions are the pubic symphysis and bladder, while the area spans multiple anatomical regions, including the prostate.

Input Ablation.— Input ablation experiments were conducted to identify anatomical regions critical to the model’s performance (Table 4). All input ablation test results were significantly different from the baseline result. Occluding both prostate and bladder regions in MR (*Organ-masked-MR* and *Box-masked-MR*) shows a significant drop in the performance, indicating that prostate, bladder, and surrounding box regions contain important RT-related changes. *Box-masked-MR* caused greater performance degradation than *Organ-masked-MR*, possibly suggesting the significance of shape changes in model prediction, which motivated the evaluation of *Mask* input.

Preservation experiments show the effect of organ shape and texture as input (*Only-organ-MR*) and only shape as input (*Mask*). Using masks alone (*Mask*) reduced performance relative to *Only-organ-MR*, although accuracy remained above 0.9 (F_1-F_L model) and 0.8 (*All-pairs* model). Prostate mask had a larger impact than bladder mask. The results suggest that prostate size is a major contributor, but intensity also contributes. The performance degradation relative to the baseline was greater for *All-pairs* model than F_1-F_L model, indicating that shape and texture information are essential to capture subtle inter-fraction changes.

All-pairs model performed best when both prostate and bladder were preserved, whereas F_1-F_L model achieved higher performance when only prostate was preserved. This indicates that the most pronounced changes between pre- and post-treatment are localized to the prostate, whereas more subtle inter-fraction changes involve both prostate and bladder.

Expert Saliency-Restricted-MR Evaluation.— The expert additionally assessed the model’s saliency maps through performing a prediction test on *saliency-restricted MR* images (Prediction Test on Saliency-Restricted-MR in Figure 1C). Although the FOV of the images is limited, the expert achieved an accuracy of 0.72 (95% CI: 0.66–0.79), showing relevance of model-highlighted regions for capturing changes.

For full volume prediction test, the expert specified the decision criteria in descending order of importance: (1) darkening of the prostate, (2) reduced distinction between the peripheral zone and transition zone borders, (3) enlargement of the prostate, and (4) reduced definition of the prostate’s outer edge. The expert primarily relied on changes in prostate volume and MR image characteristics,

| Input Type | Organ | F_1-F_L model | | All-pairs model | |
|-----------------|-------------------------|-------------------------------------|-------------------------------------|-------------------------------------|-------------------------------------|
| | | ACC | AUC | ACC | AUC |
| Baseline MR | - | $0.95 \pm 0.01^*$ | $0.99 \pm 0.00^*$ | $0.91 \pm 0.01^*$ | $0.97 \pm 0.00^*$ |
| Organ-masked-MR | Prostate | -0.03 \pm 0.01 | -0.01 \pm 0.00 | -0.01 \pm 0.01 | -0.00 \pm 0.00 |
| | Bladder | -0.02 \pm 0.01 | -0.01 \pm 0.00 | -0.04 \pm 0.01 | -0.02 \pm 0.00 |
| | Prostate \cup Bladder | -0.05 \pm 0.02 | -0.04 \pm 0.01 | -0.04 \pm 0.01 | -0.03 \pm 0.00 |
| Box-masked-MR | Prostate | -0.07 \pm 0.02 | -0.06 \pm 0.02 | -0.04 \pm 0.01 | -0.02 \pm 0.00 |
| | Bladder | -0.04 \pm 0.02 | -0.02 \pm 0.01 | -0.08 \pm 0.01 | -0.06 \pm 0.01 |
| | Prostate \cup Bladder | -0.20 \pm 0.02 | -0.19 \pm 0.02 | -0.25 \pm 0.01 | -0.25 \pm 0.01 |
| Only-organ-MR | Prostate | -0.03 \pm 0.02 | -0.01 \pm 0.01 | -0.10 \pm 0.01 | -0.08 \pm 0.01 |
| | Bladder | -0.09 \pm 0.02 | -0.06 \pm 0.01 | -0.14 \pm 0.01 | -0.12 \pm 0.01 |
| | Prostate \cup Bladder | -0.03 \pm 0.02 | -0.02 \pm 0.01 | -0.08 \pm 0.01 | -0.05 \pm 0.00 |
| Mask | Prostate | -0.05 \pm 0.02 | -0.04 \pm 0.01 | -0.16 \pm 0.01 | -0.15 \pm 0.01 |
| | Bladder | -0.21 \pm 0.03 | -0.22 \pm 0.03 | -0.29 \pm 0.01 | -0.30 \pm 0.01 |
| | Prostate \cup Bladder | -0.09 \pm 0.02 | -0.07 \pm 0.02 | -0.12 \pm 0.01 | -0.13 \pm 0.01 |

Note.—Values in the first row are presented as mean \pm standard deviation. All other values represent the difference from the baseline mean \pm standard deviation.

*: All cases are significantly different from the baseline results (independent two-sided t-test, $p < .0001$).

↓: Performance degradation compared to the baseline indicates strong model dependence on the targeted organ regions. The worst case is highlighted in bold.

↑: Higher performance indicates strong model dependence on the targeted organ regions. The best case is highlighted in bold.

Table 4. Input ablation.

including prostate brightness and clarity of the prostate edges. The rationales were similar for *saliency-restricted-MR* test (Supplementary Table A1).

3.4. Organ Volume and Intensity Changes in Images During RT

Changes in prostate and bladder volume and intensity between F_1 and F_L were analyzed to validate the model and expert findings (Figure 4). Prostate volume increased significantly from F_1 to F_L , whereas bladder volume decreased significantly (one-sided Welch's t-test, $p < .0001$). Both organs became darker, with the mean intensity in each region decreasing significantly from F_1 to F_L (independent one-sided t-test, $p = .02$ and $.001$, respectively). Additionally, the variance of intensity, reflecting heterogeneity, increased significantly in the prostate, whereas it decreased significantly in the bladder (one-sided independent t-test, $p = .002$ and $p < .0001$, respectively).

The observed increase in prostate volume and reduction in brightness aligns with both the model's results and the expert's assessments. These results suggest that the model's detection of inter-fractional changes may be partially explained by changes in prostate volume and intensity.

4. Discussion

In this study, we show that AI-based analysis of prostate MR-Linac images, which are primarily used to guide radiotherapy, has potential clinical value for detecting in-treatment anatomical and tissue changes.

This study characterizes therapy-induced changes in MR-Linac images across fractions over short time scales—one or a few days between consecutive fractions. Analyzing changes in MR-Linac images is challenging and has received limited attention, as many inter-fraction changes are subtle and difficult to detect visually. We not only developed an AI model that accurately predicts the temporal order of MR images acquired during MR-Linac treatment fractions separated by one to several days apart, but also conducted extensive evaluations—including model input ablation and clinician assessments—to investigate in-treatment changes and validate the model's clinical relevance.

The model achieved near-perfect performance, surpassing expert assessment, suggesting the presence of subtle differences that are challenging to detect visually (Table 2). Performance increased with inter-fraction interval, consistent with cumulative radiation effects (Figure 2). No significant performance difference was observed between patients with and without ADT, suggesting that RT was the

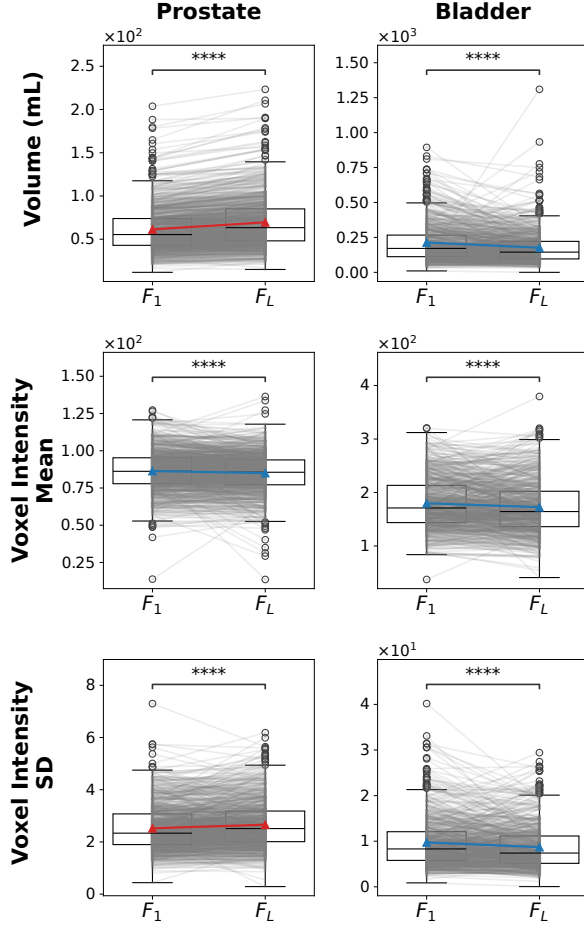


Figure 4. Changes in volume and intensity of prostate and bladder in MR images. An increase in the difference between the two means is indicated in red, whereas a decrease is indicated in blue. Stars indicate statistical significance of the difference (Wilcoxon signed-rank test; ****: $p \leq .0001$)

primary driver of the model’s decisions. Failure cases occurred primarily in consecutive fraction pairs and did not correspond to any identifiable patient characteristics (e.g., ADT) or imaging parameters (e.g., slice thickness).

Anatomical regions detected by the model were investigated through saliency maps and input ablation. The saliency maps mainly highlighted the pubic symphysis, bladder, and prostate (Table 3, Figure 3). This is consistent with reports that some patients who had radiotherapy or MR-Linac treatment for prostate cancer experience genitourinary symptoms such as urinary frequency, urethral stricture, and cystitis [16, 21, 28]. While less has been reported on the pubic symphysis, pubic bone osteomyelitis and changes in T2- and T1-weighted signals of the involved pubic rami were reported in patients who had RT for prostate cancer [24]. The result suggests that the AI model highlights RT-affected regions, including unexpected side effects, supporting its potential use in treatment assessment.

Input ablation revealed that the prostate is the primary contributor to the prediction and the bladder and surrounding regions (bounding boxes) of both organs also contribute, indicating that these areas are affected by RT. While organ size is the dominant factor, MR intensity also plays a role. The model primarily leveraged changes in the prostate and bladder for inter-fraction predictions, with pre- to post-treatment differences most pronounced in the prostate.

Quantitative analysis confirmed that the prostate enlarged and darkened with increased intensity heterogeneity, while the bladder shrank, darkened, and intensity became more uniform (Figure 4). RT may have contributed to prostate enlargement and associated bladder compression, possibly reflecting treatment-related inflammatory changes. Signal darkening occurred in both, but increased intensity variability was observed only in the prostate, suggesting differential tissue responses to targeted versus non-targeted radiation.

When the expert conducted the same test on *saliency-restricted-MR* images, the expert yielded performance significantly different from the baseline result but above chance, indicating that the model’s saliency maps capture some information about inter-fractional changes. The expert primarily relied on prostate features—volume, darkening, and edge clarity (Table A1), whereas the model also emphasized regions around the bladder and pubic symphysis (Table 3, Figure 3), suggesting it may detect additional subtle changes not readily observed by humans.

Several limitations should be acknowledged. Grad-CAM may yield broad activation patterns; fine-grained explainability methods could improve localization. This proof-of-concept used data from a single platform, and performance on other platforms remains to be determined.

In conclusion, this investigation provides conclusive evidence that AI can accurately determine the temporal order of treatment scans, suggesting the feasibility of AI-based detection of in-treatment changes as a potential biomarker of treatment response or adverse effects. Future work will serve to evaluate the ability of the model to predict biochemical failure and the development of adverse effects with the goal of appropriately selecting patients for primary and adjuvant therapy.

References

- [1] S.E. Alexander, H.A. McNair, U. Oelfke, R. Huddart, J. Murray, A. Pathmanathan, P. Patel, K. Sritharan, N. Van As, and A.C. Tree. Prostate Volume Changes during Extreme and Moderately Hypofractionated Magnetic Resonance Image-guided Radiotherapy. *Clinical Oncology*, 34(9):e383–e391, 2022.
- [2] Ahmad Algohary, Mohammad Alhusseini, Adrian L. Breto, Deukwoo Kwon, Isaac R. Xu, Sandra M. Gaston, Patri-

cia Castillo, Sanoj Punnen, Benjamin Spieler, Matthew C. Abramowitz, Alan Dal Pra, Oleksandr N. Kryvenko, Alan Pollack, and Radka Stoyanova. Longitudinal Changes and Predictive Value of Multiparametric MRI Features for Prostate Cancer Patients Treated with MRI-Guided Lattice Extreme Ablative Dose (LEAD) Boost Radiotherapy. *Cancers*, 14(18):4475, 2022.

[3] Haidara Almansour, Fritz Schick, Marcel Nachbar, Saif Afat, Victor Fritz, Daniela Thorwarth, Daniel Zips, Felix Bertram, Arndt-Christian Müller, Konstantin Nikolaou, Ahmed E Othman, and Daniel Wegener. Longitudinal monitoring of Apparent Diffusion Coefficient (ADC) in patients with prostate cancer undergoing MR-guided radiotherapy on an MR-Linac at 1.5 T: a prospective feasibility study. *Radiology and Oncology*, 57(2):184–190, 2023.

[4] Yoshua Bengio, Jérôme Louradour, Ronan Collobert, and Jason Weston. Curriculum learning. In *Proceedings of the 26th Annual International Conference on Machine Learning*, pages 41–48, Montreal Quebec Canada, 2009. ACM.

[5] Jane Bromley, Isabelle Guyon, Yann LeCun, Eduard Säckinger, and Roopak Shah. Signature verification using a “siamese” time delay neural network. In *Advances in Neural Information Processing Systems*, pages 737–744, 1994.

[6] S. Chopra, R. Hadsell, and Y. LeCun. Learning a similarity metric discriminatively, with application to face verification. In *2005 IEEE Computer Society Conference on Computer Vision and Pattern Recognition (CVPR'05)*, pages 539–546. IEEE.

[7] Olga Maria Dona Lemus, Minsong Cao, Bin Cai, Michael Cummings, and Dandan Zheng. Adaptive Radiotherapy: Next-Generation Radiotherapy. *Cancers*, 16(6):1206, 2024.

[8] Nitara Fernando, Tony Tadic, Winnie Li, Tirth Patel, Jerusha Padayachee, Anna T. Santiago, Jennifer Dang, Peter Chung, Enrique Gutierrez, Catherine Coolens, Edward Taylor, and Jeff D. Winter. Repeatability and reproducibility of prostate apparent diffusion coefficient values on a 1.5 T magnetic resonance linear accelerator. *Physics and Imaging in Radiation Oncology*, 30:100570, 2024.

[9] Pavla Hanzlikova, Dominik Vilimek, Radana Vilimkova Kankova, Martina Ladrova, Valeria Skopelidou, Zuzana Ruzickova, Radek Martinek, and Jakub Cvek. Longitudinal analysis of T2 relaxation time variations following radiotherapy for prostate cancer. *Helijon*, 10(2):e24557, 2024.

[10] Kaiming He, Xiangyu Zhang, Shaoqing Ren, and Jian Sun. Deep residual learning for image recognition. In *Proceedings of the IEEE Conference on Computer Vision and Pattern Recognition (CVPR)*, 2016.

[11] Fabian Isensee, Paul F Jaeger, Simon AA Kohl, Jens Petersen, and Klaus H Maier-Hein. nnu-net: a self-configuring method for deep learning-based biomedical image segmentation. *Nature methods*, 18(2):203–211, 2021.

[12] Heejong Kim and Mert R. Sabuncu. Learning to compare longitudinal images. <https://arxiv.org/abs/2304.02531>, 2023. arXiv:2304.02531.

[13] Heejong Kim, Batuhan K. Karaman, Qingyu Zhao, Alan Q. Wang, Mert R. Sabuncu, and for the Alzheimer’s Disease Neuroimaging Initiative. Learning-based inference of longitudinal image changes: Applications in embryo development, wound healing, and aging brain. *Proceedings of the National Academy of Sciences*, 122(8):e2411492122.

[14] Diederik P. Kingma and Jimmy Ba. Adam: A Method for Stochastic Optimization, 2014.

[15] Winnie Li, Jeff Winter, Jerusha Padayachee, Jennifer Dang, Vickie Kong, and Peter Chung. Case Report: MR-Guided Adaptive Radiotherapy, Some Room to Maneuver. *Frontiers in Oncology*, 12:877452, 2022.

[16] Xin Liu, Zhenjiang Li, and Yong Yin. Clinical application of MR-linac in tumor radiotherapy: a systematic review. 18(1): 52.

[17] Annika Mannerberg, Emilia Persson, Joakim Jonsson, Christian Jamtheim Gustafsson, Adalsteinn Gunnlaugsson, Lars E. Olsson, and Sofie Ceberg. Dosimetric effects of adaptive prostate cancer radiotherapy in an MR-linac workflow. *Radiation Oncology*, 15(1):168, 2020.

[18] Nicolas Mottet, Joaquim Bellmunt, Michel Bolla, Erik Briers, Marcus G. Cumberbatch, Maria De Santis, Nicola Fossati, Tobias Gross, Ann M. Henry, Steven Joniau, Thomas B. Lam, Malcolm D. Mason, Vsevolod B. Matveev, Paul C. Moldovan, Roderick C.N. Van Den Bergh, Thomas Van Den Broeck, Henk G. Van Der Poel, Theo H. Van Der Kwast, Olivier Rouvière, Ivo G. Schoots, Thomas Wiegel, and Philip Cornford. EAU-ESTRO-SIOG Guidelines on Prostate Cancer. Part 1: Screening, Diagnosis, and Local Treatment with Curative Intent. *European Urology*, 71 (4):618–629, 2017.

[19] Jure Murgić. MRI-Guided Radiotherapy for Prostate Cancer: a New Paradigm. *Acta Clinica Croatica*, 2022.

[20] John Ng, Fabiana Gregucci, Ryan T. Pennell, Himanshu Nagar, Encouse B. Golden, Jonathan P. S. Knisely, Nicholas J. Sanfilippo, and Silvia C. Formenti. MRI-LINAC: A transformative technology in radiation oncology. *Frontiers in Oncology*, 13:1117874, 2023.

[21] Carla Pisani, Andrea Galla, Gianfranco Loi, Debora Beldi, and Marco Krengli. Urinary toxicity in patients treated with radical EBRT for prostate cancer: Analysis of predictive factors in an historical series. 109(7):826–833.

[22] James W. Randall, Nikhil Rammohan, Indra J. Das, and Poonam Yadav. Towards Accurate and Precise Image-Guided Radiotherapy: Clinical Applications of the MR-Linac. *Journal of Clinical Medicine*, 11(14):4044, 2022.

[23] Ramprasaath R. Selvaraju, Michael Cogswell, Abhishek Das, Ramakrishna Vedantam, Devi Parikh, and Dhruv Batra. Grad-CAM: Visual Explanations From Deep Networks via Gradient-Based Localization. pages 618–626, 2017.

[24] Stephanie J. Sexton, Garjae Lavien, Nicholas Said, William Eward, Andrew C. Peterson, and Rajan T. Gupta. Magnetic resonance imaging features of pubic symphysis urinary fistula with pubic bone osteomyelitis in the treated prostate cancer patient. 44(4):1453–1460.

[25] Jan-Jakob Sonke, Marianne Aznar, and Coen Rasch. Adaptive Radiotherapy for Anatomical Changes. *Seminars in Radiation Oncology*, 29(3):245–257, 2019.

[26] Nicholas J. Tustison, Philip A. Cook, Andrew J. Holbrook, Hans J. Johnson, John Muschelli, Gabriel A. Devenyi, Jeffrey T. Duda, Sandhitsu R. Das, Nicholas C.

Cullen, Daniel L. Gillen, Michael A. Yassa, James R. Stone, James C. Gee, and Brian B. Avants. The ANTsX ecosystem for quantitative biological and medical imaging. *Scientific Reports*, 11(1):9068, 2021.

[27] Yu-Feng Wang, Sirisha Tadimalla, Niluja Thiruthaneshwaran, Lois Holloway, Sandra Turner, Amy Hayden, Mark Sidhom, Jarad Martin, and Annette Haworth. Longitudinal quantitative MRI in prostate cancer after radiation therapy with and without androgen deprivation therapy. *Magnetic Resonance Imaging*, 122:110431, 2025.

[28] Thomas Willigenburg, Joanne M. Van Der Velden, Cornel Zachiu, Frederik R. Teunissen, Jan J.W. Lagendijk, Bas W. Raaymakers, Johannes C.J. De Boer, and Jochem R.N. Van Der Voort Van Zyp. Accumulated bladder wall dose is correlated with patient-reported acute urinary toxicity in prostate cancer patients treated with stereotactic, daily adaptive MR-guided radiotherapy. 171:182–188.

AI-Based Detection of In-Treatment Changes from Prostate MR-Linac Images

Supplementary Material

A1. Patient screening

Of the 1,071 patients, those who underwent multiple treatment sets ($n = 57$) and those without a prostate or prostate mask ($n = 253$) were excluded (Supplementary Figure A1), as their imaging characteristics may differ from the rest of the cohort.

A2. Segmentation of Organs in MR Images from MR-Linac Fractions

The prostate, bladder, and rectum are routinely contoured in RT guide images obtained before treatment by radiation oncologists for treatment planning purposes. Since contouring is routinely performed only on the guide images, we trained an nnU-Net [11] on the guide images to get prostate, bladder, and rectum masks in MR images from MR-Linac fractions. We assumed that the model would generalize to images from fractions, as both were obtained from the same MR-Linac system and target the same anatomical regions with consistent imaging protocols.

The segmentation model was trained, validated, and tested using split datasets of guide MR images with corresponding prostate, bladder, and rectum masks delineated by radiation oncologists. On the test set, the Dice scores of the model were 0.85, 0.95, and 0.82 for prostate, bladder, and rectum. The trained model was then applied to MR images acquired during MR-Linac treatment fractions to generate organ masks. Partial qualitative evaluation of the resulting masks, together with quantitative comparison between the trained MR-Linac temporal-ordering models, demonstrated that this approach outperformed masks obtained via image registration.

We used dilated masks for input ablation experiments, except for the mask-only condition, to ensure that organ boundaries were included in the occluded or preserved regions. Binary masks were morphologically dilated by two voxels in all directions using a 3D 26-connected structuring element.

A3. Model Architecture Details

The overall framework (Figure 1B) is based on learning-based inference of longitudinal image changes (LILAC) [13], which extracts biologically meaningful temporal changes directly from paired longitudinal images. It has shown effectiveness across multiple longitudinal imaging applications, including embryo development, wound healing, brain aging, and Alzheimer’s disease. Adapting the LILAC framework, we employed a convolutional neu-

ral network (ResNet-18 [10]) with a Siamese architecture [5, 6, 12], which takes a pair of images as input and extracts the corresponding feature representations to predict the correct order of the given longitudinal image pair. For Siamese architecture, ResNet-18 [10] with 3D convolutional layers was used, which demonstrated superior performance compared to simple convolutional neural networks (Supplementary Table A2). The difference between these feature vectors is subsequently fed to a bias-free fully connected layer, enabling the model to learn differences between the two images. The resulting logits are used for binary classification to determine whether the input pair is in the correct or reversed temporal order using the binary cross-entropy loss function.

A4. Training Details

For the temporal-ordering task on image pairs, MR images from fractions were paired in all possible permutations with repetition. Consequently, n^2 image pairs were generated per patient (n : the number of fractions for the patient). In total, this pairing yielded 2,238 pairs for the training data, 737 pairs for the validation data, and 732 pairs for the test data. Ground truth labels were assigned as 1 for the temporally ordered, 0 for the temporally reversed, and 0.5 for the identical pairs.

A curriculum learning approach was adopted as part of the training strategy [4], where a model is gradually exposed to examples in an order from easy to hard to improve learning efficiency and performance. The approach resulted in improved performance compared with training from scratch (Supplementary Table A2).

Models were trained for 100 epochs, with the optimal epoch identified as the one yielding the smallest validation loss. Training and validation losses were monitored to check for convergence and overfitting. Model parameters were optimized using the Adam optimizer [14] to minimize the binary cross-entropy loss between the model outputs and the ground truth. The learning rate was initially set to 0.001 and decayed by a factor of 0.5 every 20 epochs. Training was conducted using the *Python PyTorch* library on a NVIDIA A40 GPU.

A5. Linear Mixed-Effects model

A linear mixed-effects model was constructed to relate the positive fraction intervals from the first fraction in F_1-F_X ($X > 1$) pairs and the corresponding model logits. Because there was no change when comparing the initial time point to itself, intercepts were omitted from the linear mixed-

effects model, and only subject-specific random slopes were included. The significance of individual variability was evaluated using a likelihood ratio test comparing the full model with random effects to a reduced model without them.

A6. Grad-CAM

A modified Gradient-weighted Class Activation Mapping (Grad-CAM) [13, 23] was calculated to obtain the saliency maps, which visualize the areas in inputs on which the model largely depends for prediction. Gradients of the model outputs were computed with respect to the final activation maps, and importance was assigned at each spatial location individually. The activation maps were then weighted element-wise by the corresponding gradients to produce the saliency maps. Regions with high Grad-CAM values were analyzed to identify areas likely affected by MR-Linac RT.

For group-level visualization of the saliency maps, F_1 atlas was constructed from all patients in the test data using `ants.registration.build_template` module in *ANTsPy* [26], python implementation of Advanced Normalization Tools (ANTs). The module begins with an initial template, which is the average of all images. All images were nonlinearly registered using SyN (Symmetric Normalization)—ANTs’ diffeomorphic registration model—without rigid or affine alignment, over three iterations. At each iteration, warped images were averaged and blended with the previous template using a blending weight of 0.75 to ensure stable convergence, with deformation updates controlled by a gradient step of 0.2, yielding an unbiased diffeomorphic mean representation of the cohort. Using the constructed atlas, patient-wise saliency maps were transformed into the atlas space, averaged across images, and overlaid for visualization (Figure 3).

A7. Saliency-Restricted-MR Details

Binary masks were generated by thresholding the min-max scaled saliency maps at 0.3. Using these masks, we created bounding boxes that encompassed the thresholded regions. The resulting cropped images were provided to experts for the *saliency-restricted-MR* evaluation.

A8. Statistical Analysis Details

An independent two-sided t-test (*Python* `scipy.stats.ttest_ind`) was conducted for pairwise comparisons of scores (accuracy and AUC) and patient characteristics. The Wilcoxon signed-rank test (*Python* `scipy.stats.wilcoxon`) was used to compare organ volume and intensity from F_1 to F_L .

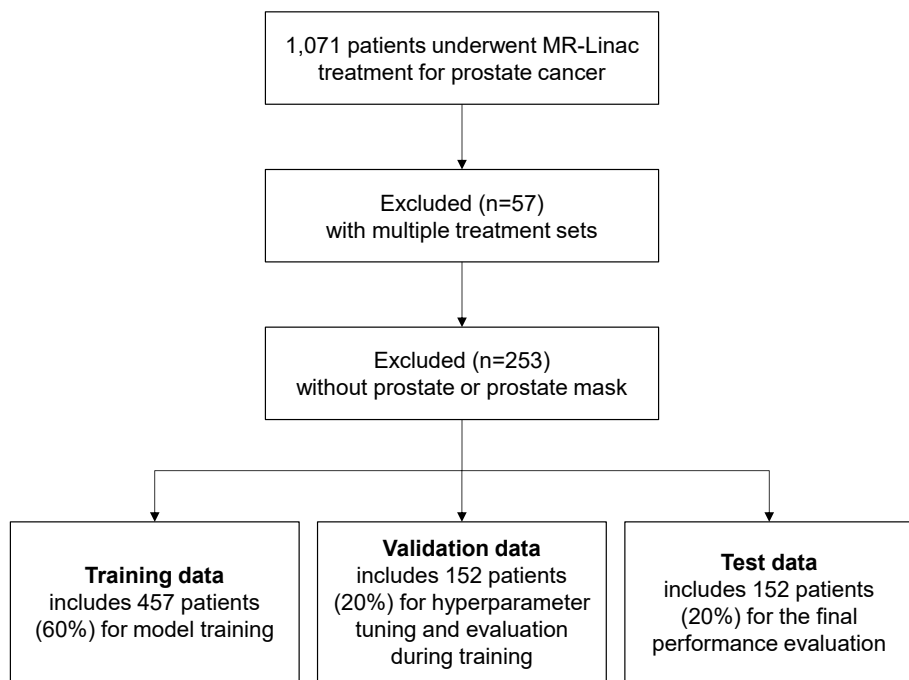


Figure A1. Flow diagram of cases, indicating inclusion and exclusion of patients, and random split of the data.

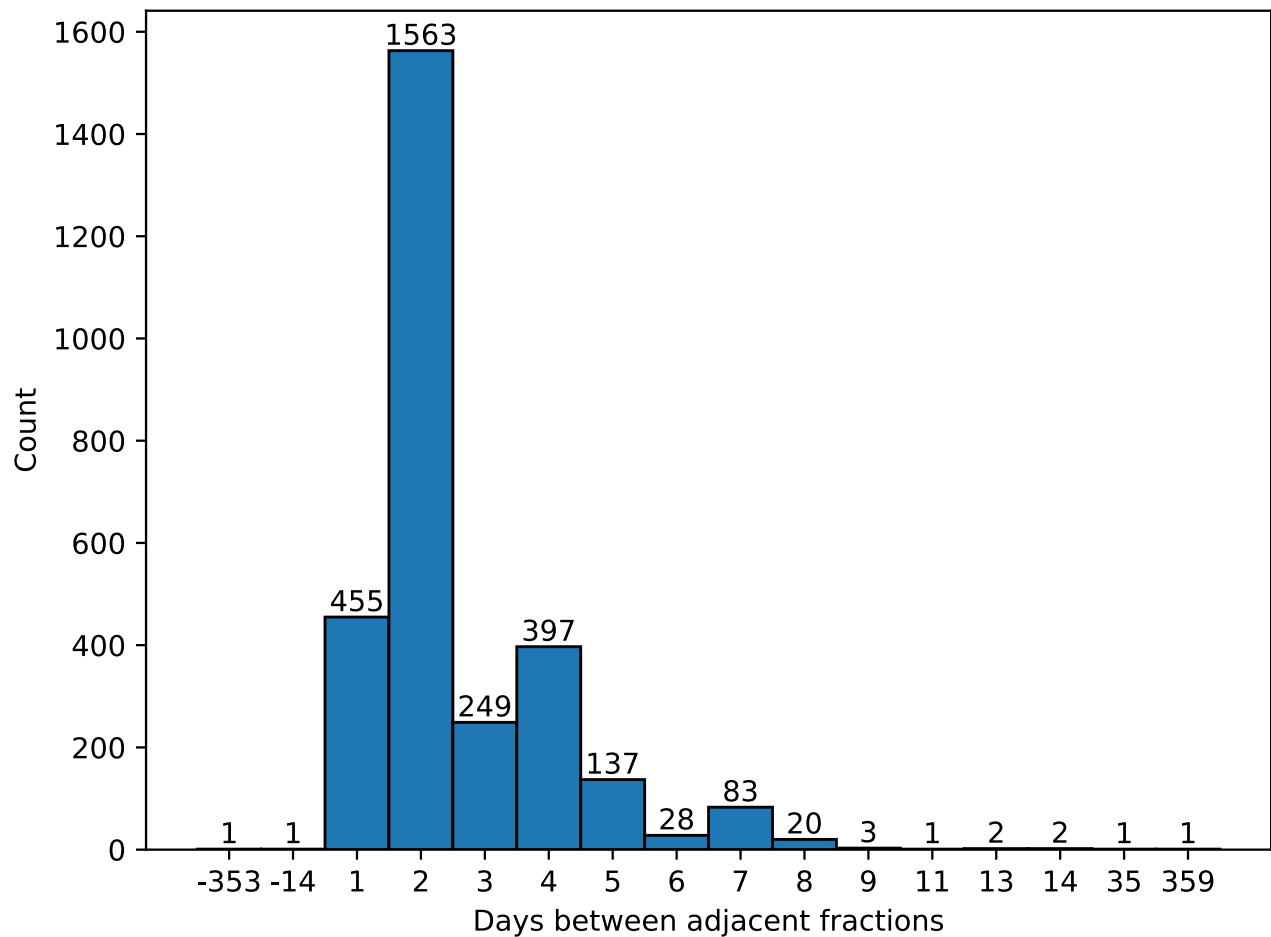


Figure A2. **Histogram of days between adjacent fractions.**

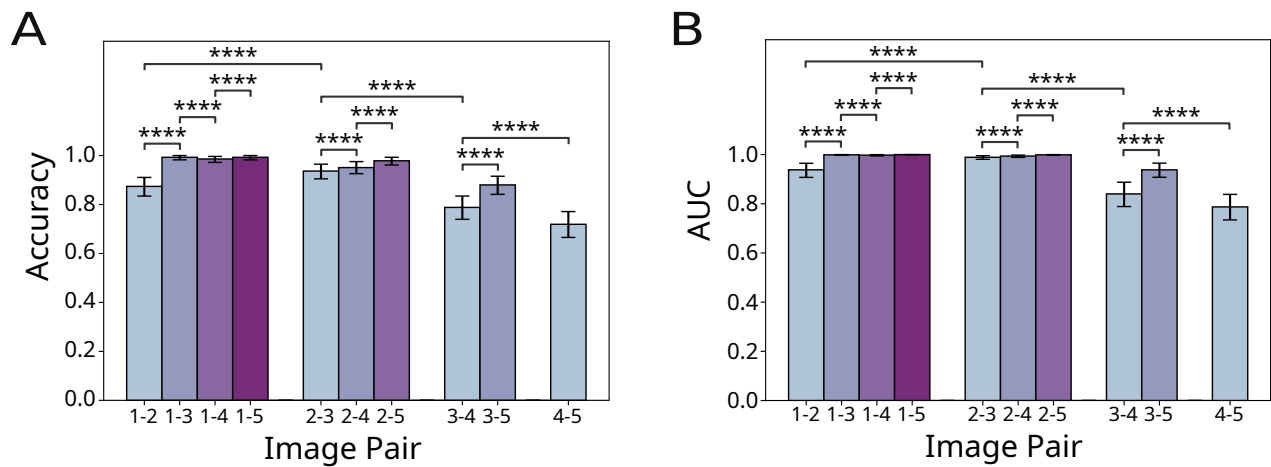


Figure A3. Pairwise performance of the *All-pairs* model. (A) Accuracy and (B) AUC of the *All-pairs* model for different image pairs. Pairs of numbers on the x-axes indicate the fractions at which the paired images were acquired. Cases were grouped by the first fraction and ordered and color-coded by the interval between the paired fractions. Stars indicate statistical significance between compared cases (independent two-sided t-test; ****: $p \leq .0001$).

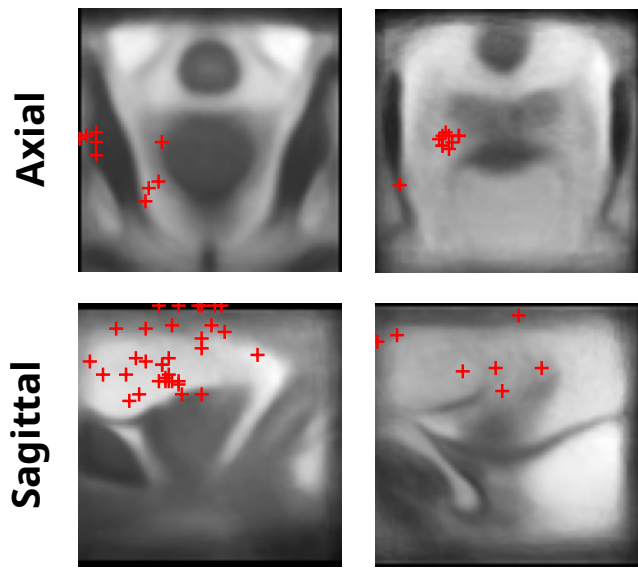


Figure A4. Peaks of saliency maps of patients in the test data on MR image atlas.

| Expert Rationale | # of Cases |
|--|------------|
| Areas in the PZ get darker. | 85 (56%) |
| Areas in the TZ get darker. | 51 (34%) |
| TZ features get indistinct. | 13 (9%) |
| Prostate missing but MR signals get darker | 2 (1%) |

Table A1. Expert rationales for temporal ordering decisions on *saliency-restricted-MR* images.

| Pair | Model & Training Scheme | ACC | AUC |
|------------|--|------|------|
| F_1-F_L | CNN-3D | 0.89 | 0.96 |
| <i>All</i> | CNN-3D, Curriculum learning from the F_1-F_L model | 0.89 | 0.96 |
| | CNN-3D, From scratch | 0.88 | 0.95 |
| | ResNet-18-3D, From scratch | 0.88 | 0.95 |

Table A2. **Performance of various models and training schemes.** CNN-3D consists of four blocks of 3D convolutional layer (number of output channels set as 16, 32, 64, 16, respectively), batch normalization, leaky ReLU, and average pooling. The ResNet-18-3D model trained with curriculum learning, which was used in the study for subsequent analyses, demonstrated superior performance compared with the CNN-3D and the ResNet-18-3D model trained from scratch.